IOWA

Reconstructed pCT Images Using Monte Carlo Simulations of a Scintillating Glass Detector

Adam Zieser[1],

Ugur Akgun[1,2], Yasar Onel[1]

[1]University of Iowa, Department of Physics & Astronomy

[2]Coe College, Physics Department

8th Annual Loma Linda Workshop

July 18-20, 2022

Outline

1) The scintillating glass calorimeter
    a) Detector design and previous work
2) Beam-oriented pCT reconstruction algorithm
3) MCNP simulations
    a) Reconstructed stopping power images
    b) Analysis
    c) Finishing thoughts

Proposal:

- A high-density, radiation hard, fluorescent glass, made with cheap reagents, to be used as the material for a scintillation detector
  - Used for in vivo range verification or pCT
- Conceived by Ugur Akgun research group at Coe College Physics department
  - Physics department specializes in glass physics/MSE
- Compact, 70 alternating layers of 100 glass bars
  - $1\ \mathrm{mm} \times 1\ \mathrm{mm} \times 10\ \mathrm{cm}$ per bar, total: $10\ \mathrm{cm} \times 10\ \mathrm{cm} \times 7\ \mathrm{cm}$
  - Resolves Bragg peak and tracking information

COE COLLEGE 1851

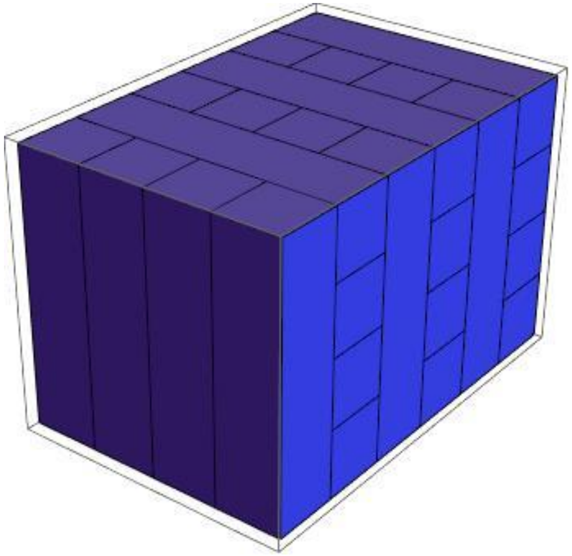

Specifications

Detector must be:

- Compact, attachable to existing proton therapy gantries
  - pCT is limited to particle rates of therapeutic pencil beams
- High-density, capable of completely stopping $\sim 200\ \mathrm{MeV}$ protons
  - Densities of $5.84\ \mathrm{g/cm^3}$ achieved in $\mathrm{Gd_2O_3 - WO_4 - B_2O_3}$ system originally explored by Taki et al.*
- Made of cheap oxides, easily manufacturable
  - $\mathrm{Eu_2O_3}$-doped glass melts at $\sim 1400\ \mathrm{C}$, standard atmosphere/pressure
  - Glass system also accepts or $\mathrm{CeCl_3}$ or $\mathrm{Tb_2O_3}$

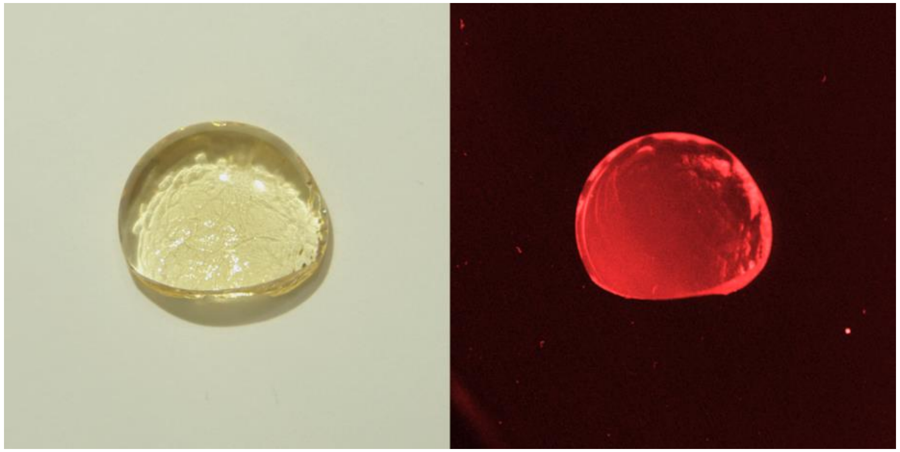

*Taki et al. Coexistence of nano-scale phase separation and micro-scale surface crystallization in Gd2O3–WO3–B2O3 glasses. *J Non Cryst Solids*, 381:17-22, 2013

Optical properties

- Experiments performed by Tillman et al.* show suitable transmission/emission properties for Eu_2O_3-doped glass
- High-wavelength emission ideal for optically-isolating coating?

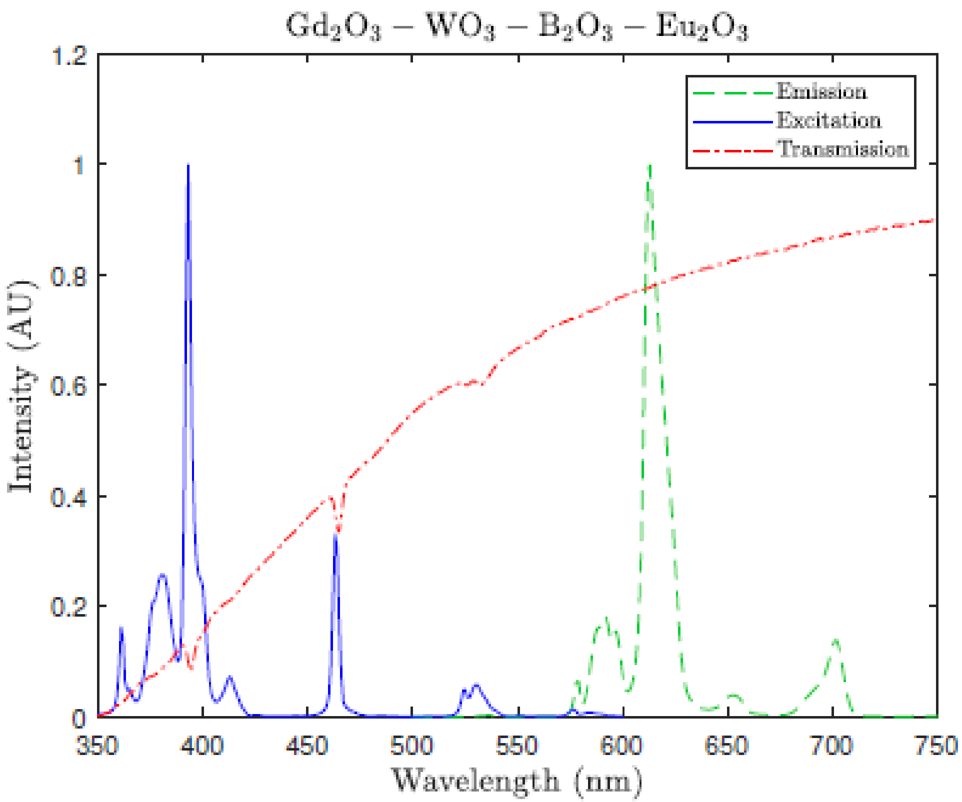

*I. J. Tillman et al. High-density scintillating glasses for a proton imaging detector. *Opt. Mater.*, 68:58-62, 2017

Previous work with the glass detector
Backup slide

- In collaboration with D. Wang (formerly Dept. of Radiation Oncology, University of Iowa), preliminary imaging results using hybrid SART/SIRT reconstruction with Geant4 simulations of Shepp-Logan phantom
  - Poor resolution, single-proton algorithm ill-suited to accelerator bunches

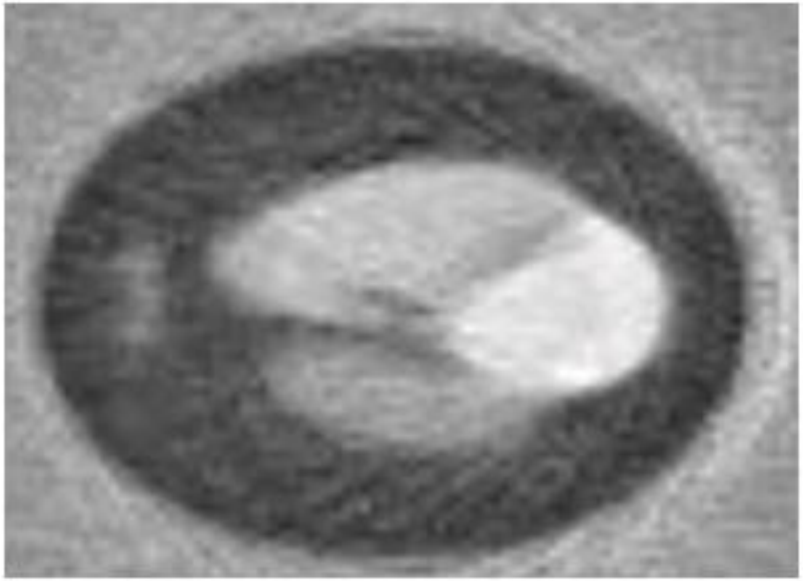

Taken from Wilkinson et al.*

*C. J. Wilkinson, L. Ruane, W. Miller, A. Gunsch, and A. Zieser. CARNA - A Compact Glass Proton Imager. In *2017 IEEE Nuclear Science Symposium and Medical Imaging Conference (NSS/MIC)*, pages 1–5. IEEE, 2017.

The problem:

- Previous imaging tests with detector have poor spatial resolution
    - Alternative reconstruction algorithm required to satisfy design constraints
- Example: Varian ProBeam isochron-cyclotron has $72.8\ \mathrm{MHz}$ RF, delivers a bunch of ~ 100 protons every $13.74\ \mathrm{ns}$ while operating at $1\ \mathrm{nA}$, with bunch length of $1-2\ \mathrm{ns}$*
    - $\sim 10\ \mathrm{ps}$ scintillator dead-time required for individual proton tracking
- Solution: use beam-oriented pCT recon methods to test detector
    - MCNP6 simulations of full pCT scans carried out to validate detector
    - Data used to reconstruct stopping power images
    - Images compared to reference truth values

*Simon Jolly et al. Technical challenges for FLASH proton therapy. *Phys. Med., 78:71-82, 2020*

Beam-oriented pCT Recon

Imaging with the glass detector

Coordinate refresher

- Beamlet parallel-projection geometry used in reconstruction and simulation
  - Rotated Euclidean $(t(y,z), s(y,z), x)$ coordinates
  - Only 2D reconstructions here
- Bragg peak placement in detector yields $\langle E_{\text{out}}^{\text{beam}} \rangle$

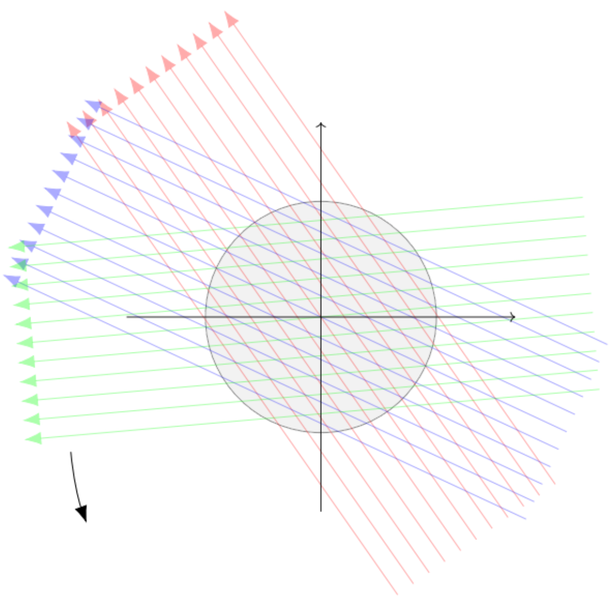

$$\begin{pmatrix} t \\ s \\ x \end{pmatrix} = \begin{pmatrix} \cos\theta & \sin\theta & 0 \\ -\sin\theta & \cos\theta & 0 \\ 0 & 0 & 1 \end{pmatrix} \begin{pmatrix} y \\ z \\ x \end{pmatrix}$$

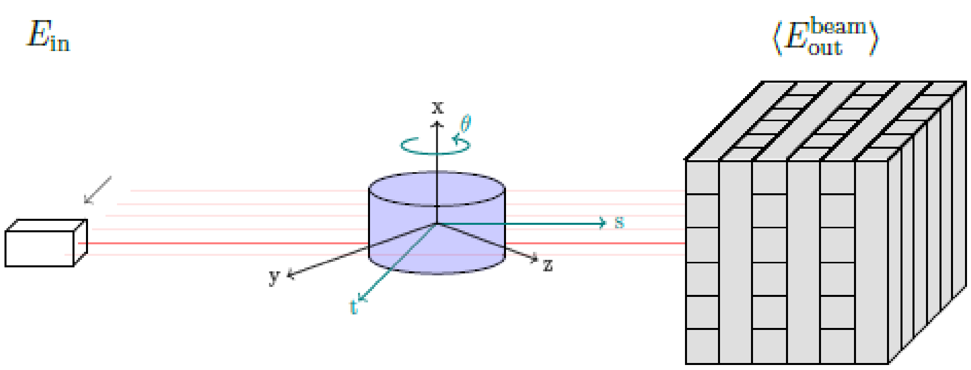

Imaging equation

- Proton imaging eq. of D. Wang et al.* modified for use with pencil beams
  - Insensitive to $\frac{S}{\rho}(I(\vec{r}), E_0) \coloneqq \frac{S}{\rho}\left(I_{\mathrm{H_2O}}, E_0\right)$ across tissues ($I_{\mathrm{H_2O}} = 75$ eV used)
  - Unknown: mean exit energy $\left\langle E_{\mathrm{out}}^{\mathrm{beam}} \right\rangle_{\mu_t}$, initial energy $\left\langle E_{\mathrm{in}}^{\mathrm{beam}} \right\rangle_{\mu_t}$, mean beam position μ_t, and mean-beam path $\langle \mathcal{L} \rangle_{\mu_t}$

$$G_\theta(\mu_t, E_0) \stackrel{\mathrm{def}}{=} -\int_{\left\langle E_{\mathrm{in}}^{\mathrm{beam}} \right\rangle_{\mu_t}}^{\left\langle E_{\mathrm{out}}^{\mathrm{beam}} \right\rangle_{\mu_t}} \left(\frac{S}{\rho}\left(I_{\mathrm{H_2O}}, E_0\right) \Big/ \frac{S}{\rho}\left(I_{\mathrm{H_2O}}, E\right) \right) \mathrm{d}E = \int_{\langle \mathcal{L} \rangle_{\mu_t}} S(\rho_e(\vec{r}), I(\vec{r}), E_0)\, \mathrm{d}\ell$$

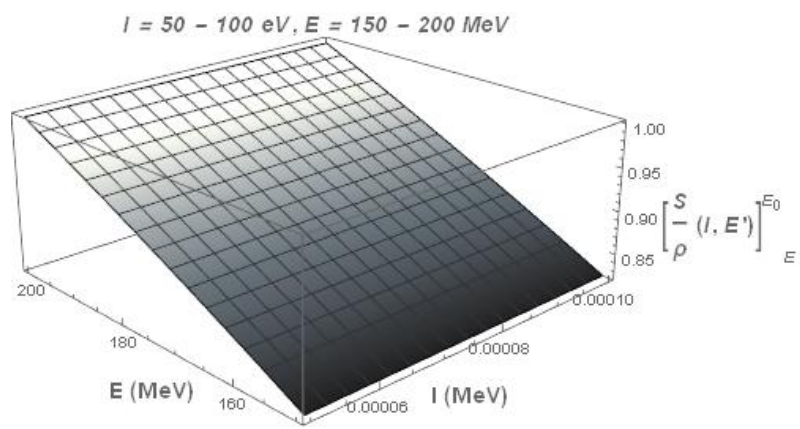

*Dongxu Wang et al. On the use of a proton path probability map for proton computed tomography reconstruction. *Med Phys,* 37(8):4138-4145, 2010

Modeling the path

Backup slide

- Beam modeling (and FBP_{BEAM} reconstruction algorithm) based on work of Rescigno et al.*
  - Beam is a spreading Gaussian, nuclear halo and aura neglected; not statistically significant enough for imaging
- Beam parameters evolve with moments of empirical differential Molière scattering power $T_{\mathrm{H_2O}}\left(pv(s)\right)$
  - Scattering properties of water are assumed everywhere

$$\Phi(\mu_t, t, s) = N(s)\frac{exp\left(= -\frac{1}{2}\frac{(t-\mu_t)^2}{\sigma_t^2(s)}\right)}{\sqrt{2\pi}\sigma_t(s)}$$

$$\sigma_t^2(s) = \sigma_t^2(0) + \frac{1}{2}\int_0^s (s-s')^2 T_{\mathrm{H_2O}}\left(pv(s')\right)ds'$$

*Regina Rescigno et al. A pencil beam approach to proton computed tomography. *Med Phys, 42(11)*:6610-6624, 2015

Recon pixel contribution

- Each beam ray $G_\theta(\mu_i, E_0)$ contributes to projections $g(t, s, E_0)$
  - Each beam Gaussian contributes $w(\mu_i, t, s)$ to a projection
  - Assumptions made for depth-evolution of $w(\mu_i, t, s)$ along s, t
  - $g(t, s, E_0)$ available at all depths s, “virtual radiographs”

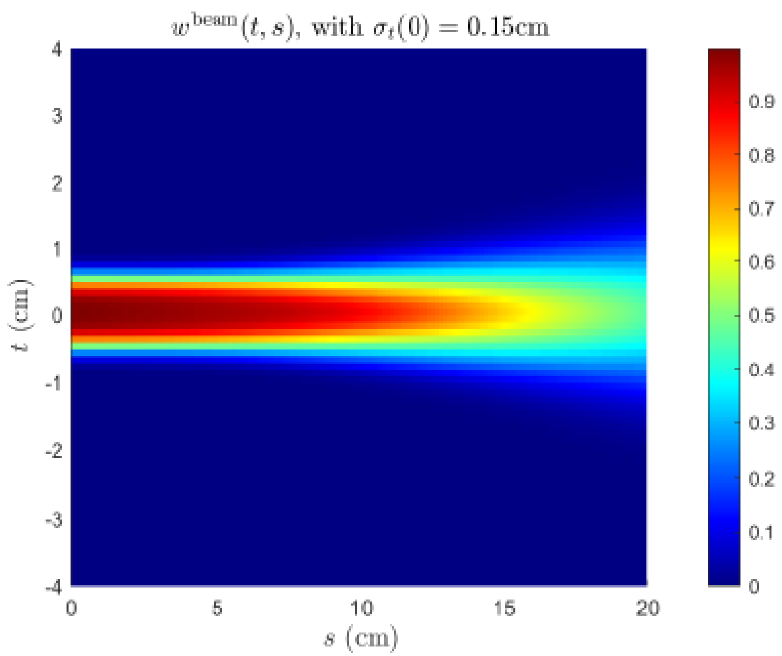

$$g(t, s, E_0) = \frac{\sum_{i \in B_\theta} w(\mu_i, t, s) G_\theta(\mu_i, E_0)}{\sum_{i \in B_\theta} w(\mu_i, t, s)}$$

$$w(\mu_i, t, s) = \int_{t-d/2}^{t+d/2} \frac{\Phi(\mu_t, t, s)}{N_0} dt$$

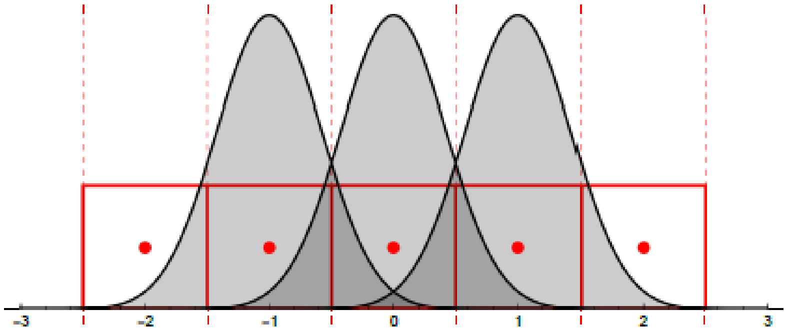

Reconstruction

Distance-driven binning

- Projections g are convoluted with a filter to form filtered projections $\mathcal{g}$
- $\mathcal{g}$ is calculated on a grid of points
  - Pixel values found with 2D linear interpolation
- Reconstructed SP is a sum of contributions from all projections

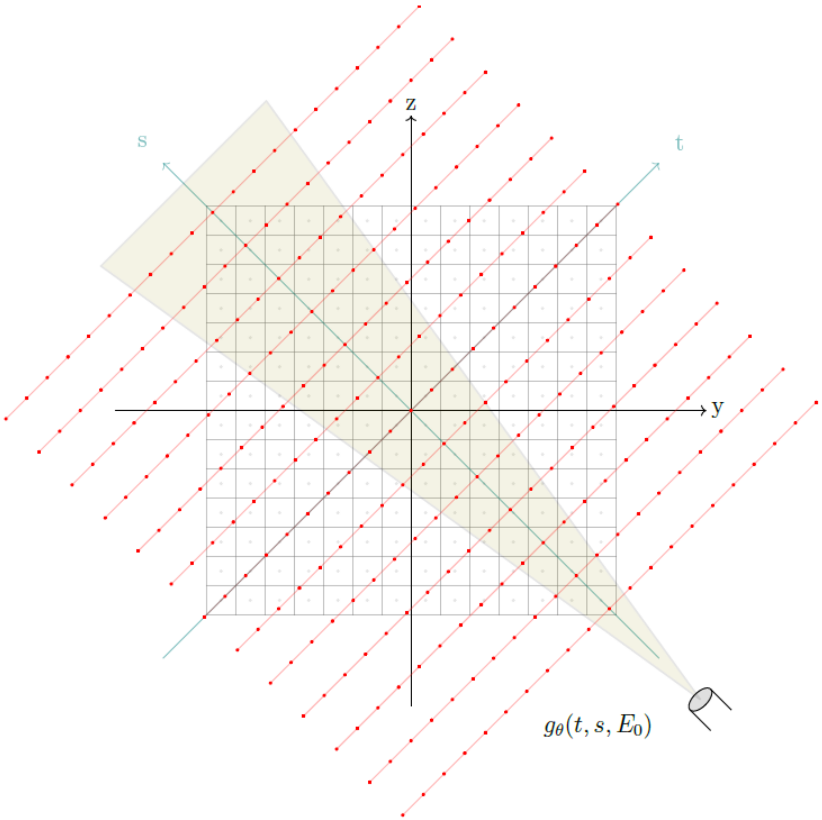

$$S(y,z,E_0) = \frac{\pi}{N_P}\sum_{\theta}^{N_P} \mathcal{g}_\theta(t(y,z), s(y,z), E_0)$$

MCNP simulations

Simulation parameters, reconstructed images, analysis

Simulated phantom

- Gammex RMI 467 tissue calibration phantom used
- Simulations performed with two phantom configurations: standard and titanium
  - Tests reconstructions with extreme beam hardening

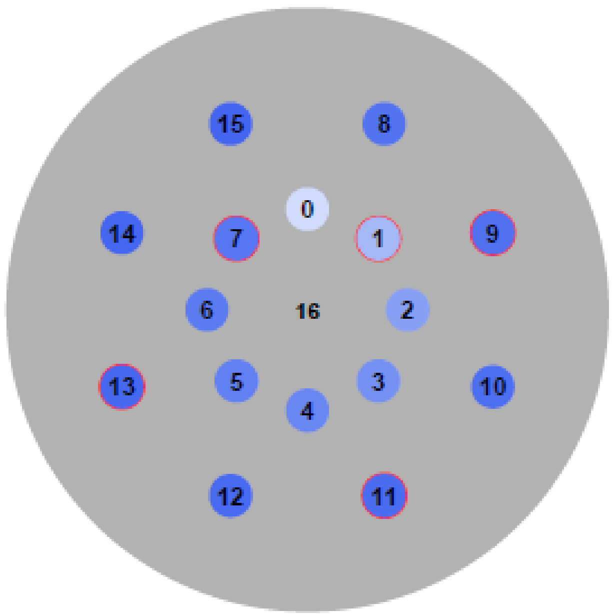

0) CB2 – 30%
1) Solid water / Ti
2) CB2 – 50%
3) AP6 Adipose
4) BRN–SR2 Brain
5) SB3 Cortical bone
6) BR–12 Breast
7) Water / Ti
8) LV1 Liver
9) Solid water / Ti
10) IB Inner Bone
11) Solid water / Ti
12) Lung 300
13) Solid water / Ti
14) Lung 450
15) B200 Bone Mineral
16) Solid Water

MCNP simulation

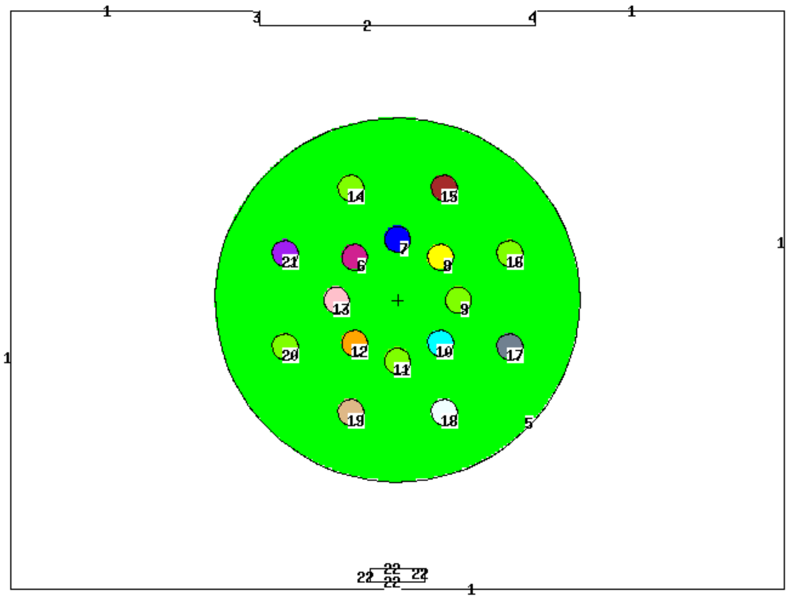

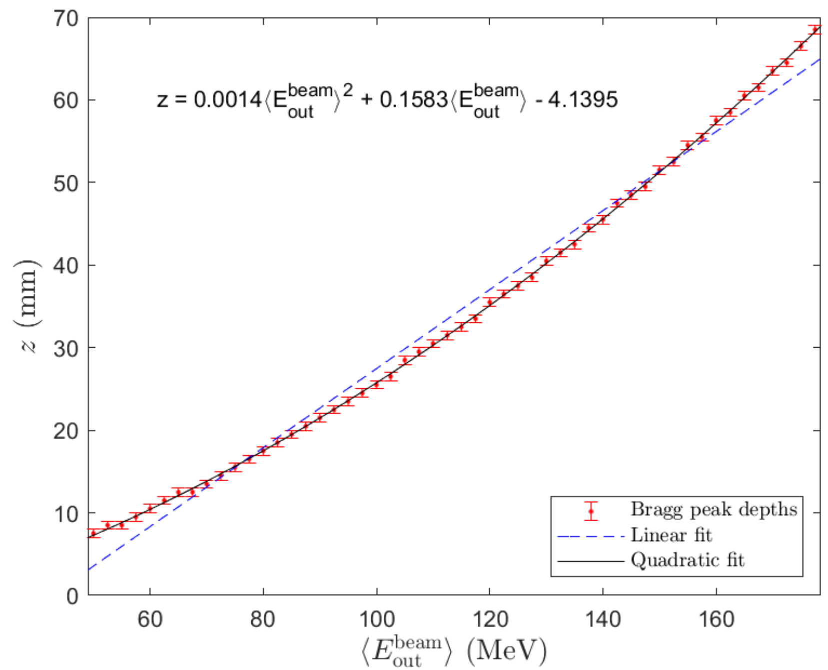

- Detector not simulated in pCT scans to save processing
  - $\langle E_{\text{out}}^{\text{beam}} \rangle = {}^{E_{\text{total}}}/_{N_{\text{total}}}$ recorded by energy flux and particle surface tally
  - Calibration curve formed to relate $s_{\text{Bragg}}(\langle E_{\text{out}}^{\text{beam}} \rangle)$
- 10^4 histories per ray, beam CCC cell truncated at 2 SD

Images

- Scans carried out for both configurations, with four beam energies $(150, 170, 190, 210\ \mathrm{MeV})$, two initial Gaussian beam widths $(\sigma_t(0) = 2.5\ \mathrm{mm}^*, 1.5\ \mathrm{mm})$
- Each has 180 projections over $360°$, 141 beams per projection
  - Images are141 x 141 pixels
  - Distance-driven binning grid of 141 x 200
- Wider beam width unfeasible

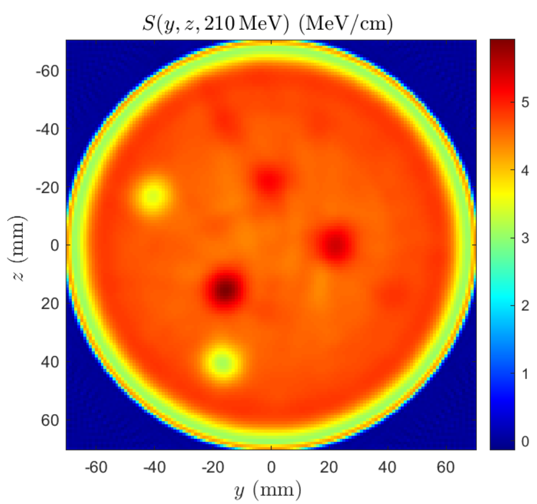

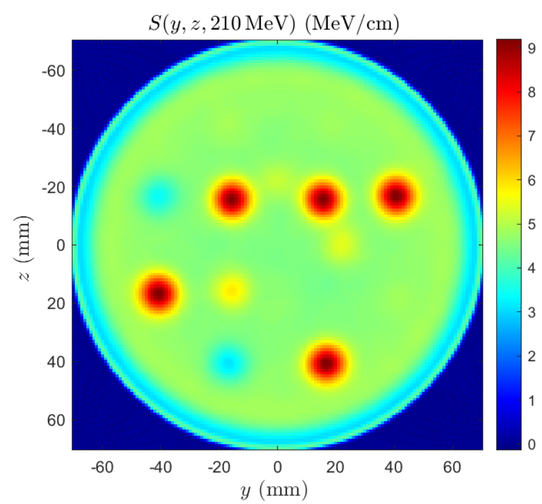

*Alexandra Moignier et al. Toward improved target conformity for two spot scanning proton therapy delivery systems using dynamic collimation, *Med Phys*, 43(3):1421-1427, 2016

Cont.

- Less artifacting, compared to standard FBP
- Extremes of $150\ \mathrm{MeV}$ and $210\ \mathrm{MeV}$ shown

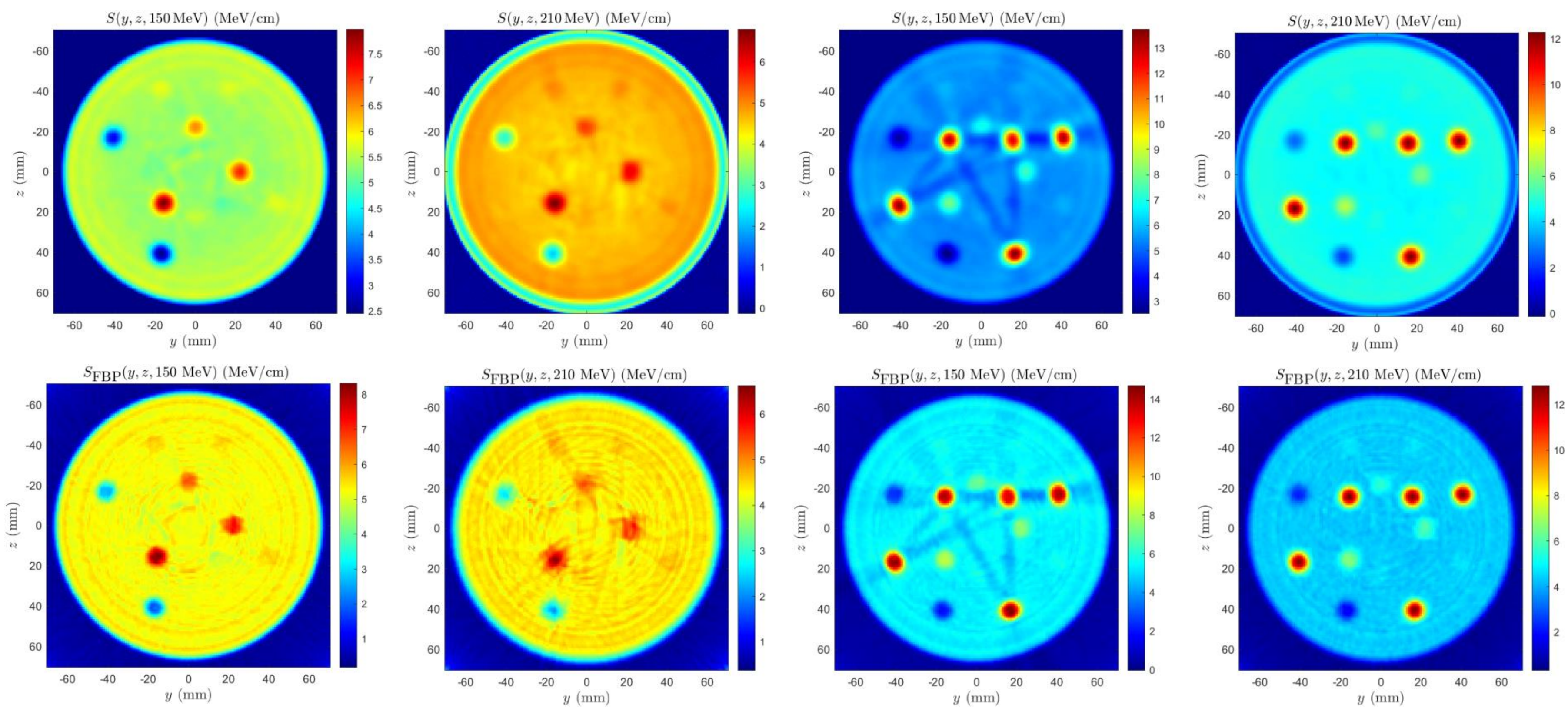

Error Analysis

- Accuracy of reconstructions compare average of pixels in inserts to reference values, S_{ref}
  - Reference values calculated from manufacturer ρ_e values, and elemental compositions: $S(\rho_e, I(Z))$
  - Contrast calculated to judge visibility against background

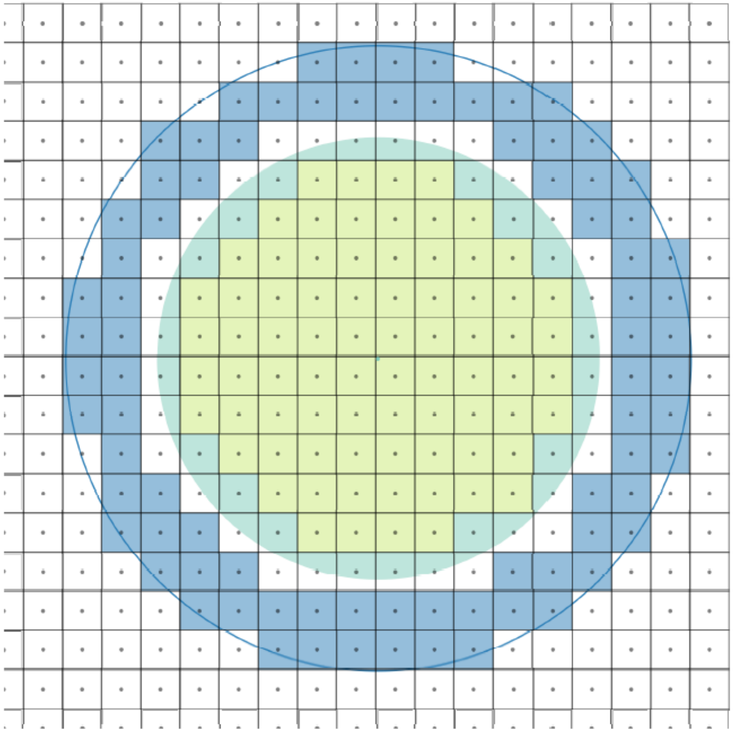

$$RE_i = \frac{\bar{S}_i - S_{\text{ref},i}}{S_{\text{ref},i}} \times 100\%$$

$$C_i = \frac{|\bar{S}_i - \bar{S}_{B,i}|}{\sqrt{\sigma_i^2 + \sigma_{B,i}^2}}$$

Error Images

- Generally low errors for water-like tissues
- Extremely high lung, bone, titanium errors
  - Product of backprojection? Present in FBP images as well

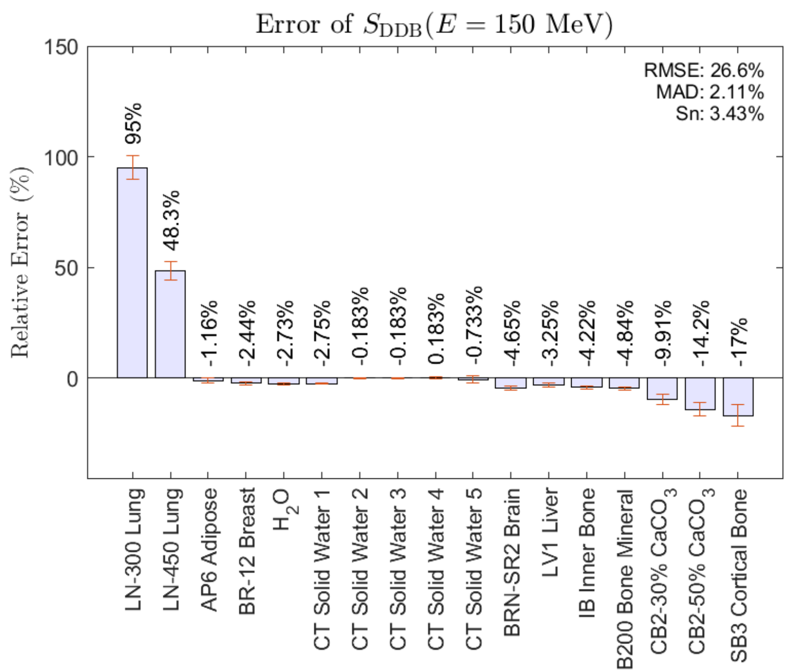

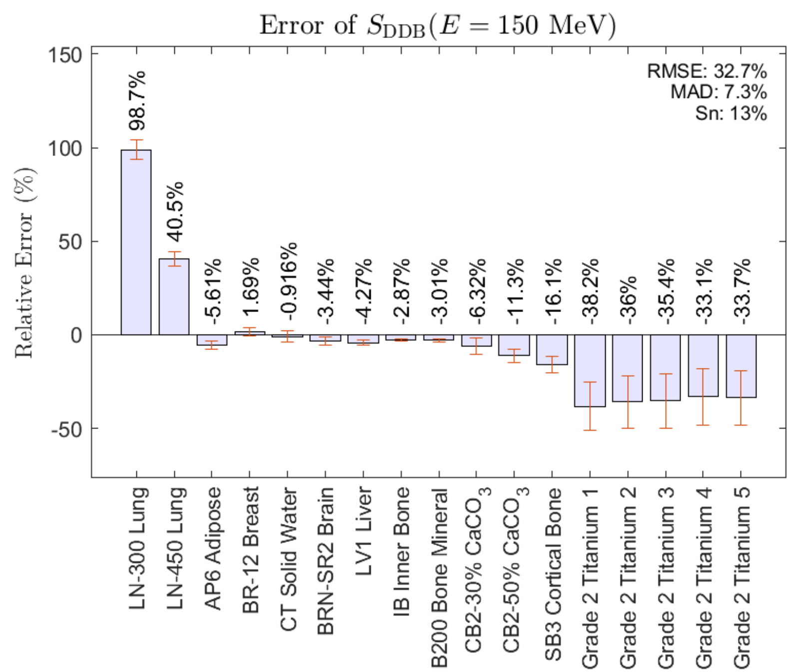

Contrast

- Contrast low for nearly water-equivalent tissues
- FBP_{BEAM} outperforms standard FBP negligibly in glass detector
- "Perfect resolution" images very similar, so shortcomings unrelated to detector resolution

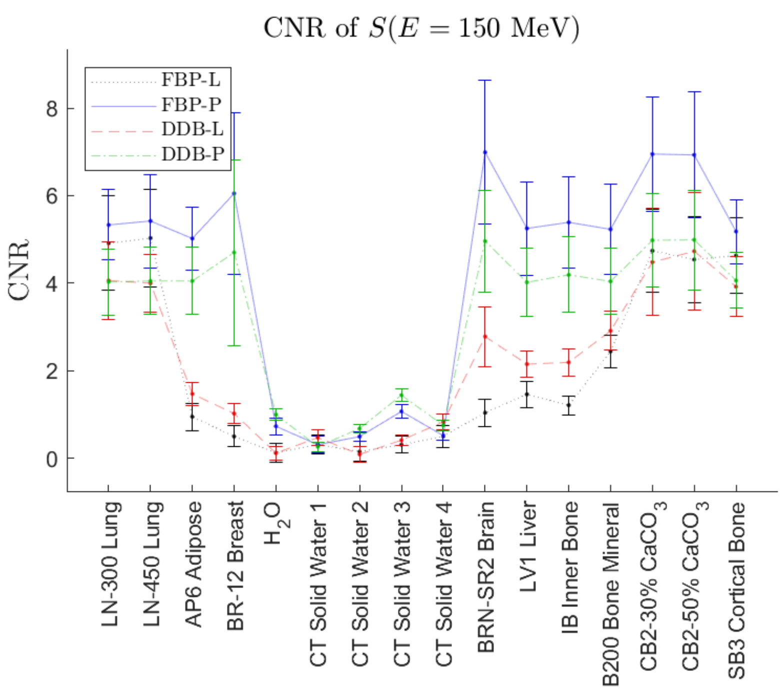

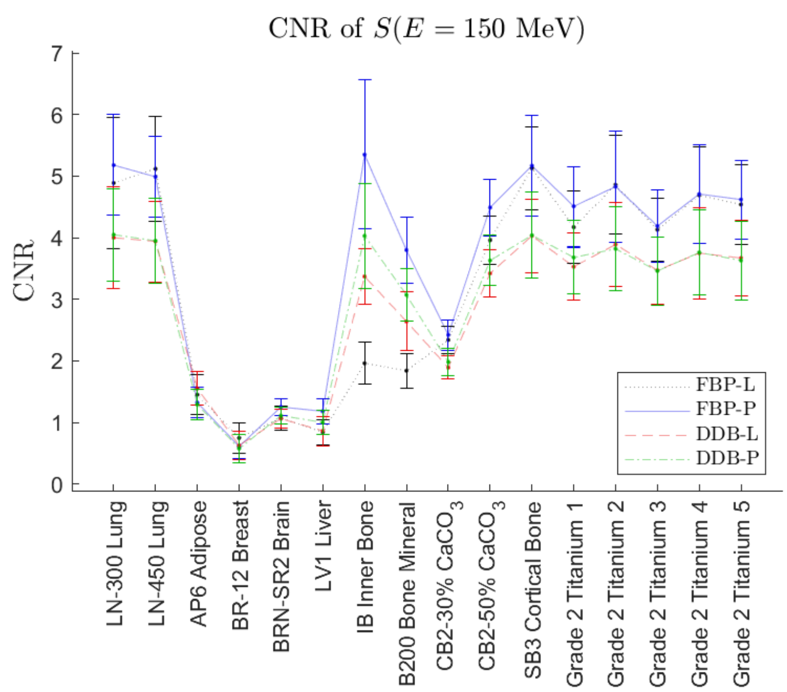

Cont.

- The FBP_{BEAM} algorithm outperforms FBP at low densities and energies, but worse at high energy and higher densities
  - Comparison via $|RE_i| - |RE_{\mathrm{FBP},i}|$ values

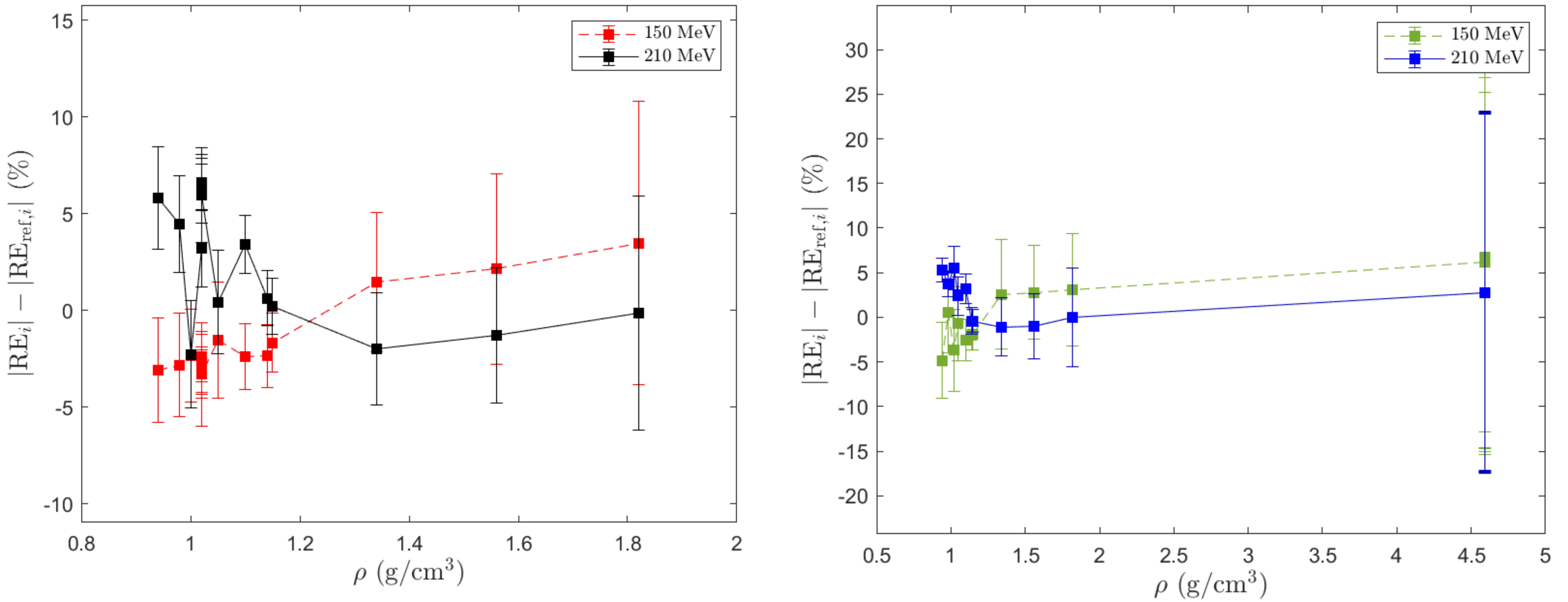

Possible future work

- Improved reconstruction algorithms
  - Current implementation of FBP-style algorithms loosely based on Matlab internal code, may not be optimal?
  - Beam-based algebraic techniques instead?
- More rays per projection for pCT scans may be necessary
  - Bragg peaks statistically significant for rays as sparse as 100 protons; more rays possible without excessive additional dose
  - Limited by precise detection of μ_t, accurate entrance tracking plane required
- Results promising, but need improvement

End

Thank you! Questions?

Adam Zieser, Ugur Akgun, and Yasar Onel. Reconstructed pCT Images Using Monte Carlo Simulations of a Scintillating Glass Detector, 2022. arXiv:2206.09993.

Previous glass detector publications

Extra slide

- G. L. Ademoski et al. A glass neutron detector with machine learning capabilities. *J. Instrum.*, 14(6):P06013–P06013, 2019. doi:10.1088/1748-0221/14/06/p06013.
- Gabriel Varney, Catherine Dema, Burak E. Gul, Collin J. Wilkinson, and Ugur Akgun. Use of machine learning in CARNA proton imager. In *Medical Imaging 2019: Physics of Medical Imaging*, volume 10948, pages 1317–1325. SPIE, 2019. doi:10.1117/12.2512565.
- C. J. Wilkinson et al. High-density scintillating glasses for a proton imaging detector. In: Medical Imaging 2017: Physics of Medical Imaging,
- C. J. Wilkinson, L. Ruane, W. Miller, A. Gunsch, and A. Zieser. CARNA - A Compact Glass Proton Imager. In *2017 IEEE Nuclear Science Symposium and Medical Imaging Conference (NSS/MIC)*, pages 1–5. IEEE, 2017. doi:10.1109/NSSMIC.2017.8533076.
- I. J. Tillman et al. High-density scintillating glasses for a proton imaging detector. *Optical Materials*, 68:58–62, 2017. doi:10.1016/j.optmat.2016.10.015.